

First principles calculation of lattice thermal conductivity in crystalline phase change materials: GeTe, Sb₂Te₃ and Ge₂Sb₂Te₅

Davide Campi^{1,2,3}, Lorenzo Paulatto⁴, Giorgia Fugallo^{4,5}, Francesco Mauri⁶, and Marco Bernasconi^{1*}

¹*Dipartimento di Scienza dei Materiali, Università di Milano-Bicocca, Via R. Cozzi 55, I-20125, Milano, Italy*

²*Theory and Simulation of Materials (THEOS), École Polytechnique Fédérale Lausanne, CH-1015 Lausanne, Switzerland*

³*National Center for Computational Design and Discovery of Novel Materials (MARVEL),
École Polytechnique Fédérale Lausanne, 1015 Lausanne, Switzerland*

⁴*Université Pierre et Marie Curie-Paris 6, CNRS, IMPMC-UMR7590,
case 115, 4 Place Jussieu, 75252 Paris Cedex 05, France*

⁵*Laboratoire des Solides Irradiés, École Polytechnique, 91128 Palaiseau Cedex, France and*

⁶*Dipartimento di Fisica, Università di Roma La Sapienza, Piazzale Aldo Moro 5, I-00185 Roma, Italy*

Thermal transport is a key feature for the operation of phase change memory devices which rest on a fast and reversible transformation between the crystalline and amorphous phases of chalcogenide alloys upon Joule heating. In this work we report on the ab-initio calculations of bulk thermal conductivity of the prototypical phase change compounds Ge₂Sb₂Te₅ and GeTe in their crystalline form. The related Sb₂Te₃ compound is also investigated for the sake of comparison. Thermal conductivity is obtained from the solution of the Boltzmann transport equation with phonon scattering rates computed within density functional perturbation theory. The calculations show that the large spread in the experimental data on the lattice thermal conductivity of GeTe is due to a variable content of Ge vacancies which at concentrations realized experimentally can halve the bulk thermal conductivity with respect to the ideal crystal. We show that the very low thermal conductivity of hexagonal Ge₂Sb₂Te₅ of about 0.45 Wm⁻¹ K⁻¹ measured experimentally is also resulting from disorder in the form of a random distribution of Ge/Sb atoms in one sublattice.

I. INTRODUCTION

Chalcogenide alloys are attracting an increasing interest for their use in optical data storage (digital versatile disk, DVDs) and, more recently, in electronic non volatile memories (Phase Change Memories, PCM)¹⁻⁵. These applications rest on a fast and reversible transformation between the amorphous and crystalline phases upon heating. The two phases can be discriminated thanks to a large contrast in their electrical conductivity (in PCMs) and optical reflectivity (in DVDs). In PCM operation, read-out of the cell resistance is performed at low bias. Programming the memory requires instead a relatively large current to heat up the active layer and to induce the phase change which can be either the melting of the crystal and subsequent amorphization or the recrystallization of the amorphous phase.

Thermal conductivity (κ) is a key property for PCM operation, as the set/reset processes strongly depend upon heat dissipation and transport⁶. Several experimental works reported on the measurements of the bulk thermal conductivity of the prototypical GeSbTe phase change alloys⁶⁻⁹ and the related binary compounds GeTe¹⁰⁻¹⁵ and Sb₂Te₃^{11,16}. These compounds have a relatively low lattice thermal conductivity in the crystalline phase which has been ascribed to a strong phonon scattering by disordered point defects.

In the case of cubic Ge₂Sb₂Te₅, which is the metastable structure the amorphous phase crystallizes into in PCM devices, disorder is present in the form of a random distribution of Ge, Sb atoms and 20 % of vacancies in one sublattice of the rocksalt structure, the other being fully occupied by Te atoms. Disorder leads to a lattice ther-

mal conductivity of $\kappa=0.40$ Wm⁻¹K⁻¹ which is close to the value of 0.27 Wm⁻¹K⁻¹ measured for the amorphous phase⁹.

In trigonal GeTe, vacancies in the Ge sublattice are responsible for the large spread of the measured thermal conductivity over the wide range of values 0.1-4.1 Wm⁻¹K⁻¹.¹⁰⁻¹⁵

The lattice thermal conductivity is very low (0.45 Wm⁻¹K⁻¹)⁹ also in the hexagonal phase of Ge₂Sb₂Te₅, the crystalline phase stable at normal conditions, in which the vacancy concentration is much lower than that of the cubic phase. In this latter case, disorder may arise from a partial random distribution of Sb/Ge atoms. Actually, the hexagonal phase of Ge₂Sb₂Te₅ has $P\bar{3}m1$ symmetry and nine atoms per unit cell in nine layers stacked along the c axis, but the distribution of atoms in the different layers are still a matter of debate in literature. Two different ordered sequences have been proposed, namely the ordered stacking Te-Sb-Te-Ge-Te-Ge-Te-Sb-Te-Te-Sb¹⁷ and the ordered stacking Te-Ge-Te-Sb-Te-Sb-Te-Ge-Te-Te-Ge¹⁸. Most recent diffraction measurements suggested, however, a disordered phase with Sb and Ge randomly occupying the same layer¹⁹ which is also confirmed by transmission electron microscopy imaging of GST nanowires²⁰.

In this work, we quantify the effect of the different types of disorder (vacancies and Ge/Sb distribution) on the lattice conductivity of hexagonal Ge₂Sb₂Te₅ and trigonal GeTe by means of density functional calculations. Phonon dispersion relations and anharmonic force constants are computed within Density Functional Perturbation Theory (DFPT)^{21,22}. Lattice thermal conductivity is then obtained from the variational solution of the

Boltzmann transport equation introduced in Ref. 23. For the sake of comparison we have also investigated thermal transport in crystalline Sb_2Te_3 which is structurally similar to $\text{Ge}_2\text{Sb}_2\text{Te}_5$ and for which the effect of disorder is marginal.

II. COMPUTATIONAL METHODS

Phonon dispersion relations were calculated by means of DFPT²¹ as implemented in the Quantum-Espresso suite of programs²⁴. We used either the Local Density Approximation (LDA) or the Perdew-Burke-Ernzerhof (PBE)²⁵ generalized gradient corrected approximation (GGA) to the exchange and correlation functional. Van der Waals (vdW) interactions, not accounted for in the GGA schemes, were also included within the scheme proposed by Grimme²⁶. Norm conserving pseudopotentials with only the outermost s and p valence electrons were used. The spin-orbit interaction was neglected since it has been shown to have negligible effects on the structural and vibrational properties of GeTe²⁷. The Kohn-Sham (KS) orbitals were expanded in a plane waves basis up to a kinetic cutoff of 30 Ry. The Brillouin Zone (BZ) integration for the self-consistent electron density was performed over Monkhorst-Pack (MP) meshes²⁸.

Third order anharmonic force constants have been computed within DFPT as described in Ref. 22. In this approach the three-phonons anharmonic coefficients for three arbitrary wave vectors ($\mathbf{q}, \mathbf{q}', \mathbf{q}''$) is computed by using the so-called $2n + 1$ theorem as formulated in Ref. 29. This scheme is presently implemented only for the LDA functional in the Quantum-Espresso package.

Phonons and anharmonic force constants are then used to solve exactly the linearized Boltzmann transport equation (BTE) by means of the variational technique introduced in Ref. 23 which we refer to for all the details. This new scheme provides a full solution of the BTE beyond the most commonly used single mode phonon relaxation time approximation (SMA) which describes rigorously the depopulation of the phonon states but not the corresponding repopulation. The momentum-conserving character of the normal (N) processes gives rise to a conceptual inadequacy of the SMA description and its use becomes questionable in the range of low temperatures where the umklapp (U) processes are frozen out and N processes dominate the phonon relaxation. The exact solution of the BTE allowed us to conclude that the SMA actually provides a good approximation for the lattice thermal conductivity at 300 K of the phase change compounds we are interested in for which the Debye temperature is actually below 300 K.

The effect of disorder in the distribution of Sb/Ge atoms in $\text{Ge}_2\text{Sb}_2\text{Te}_5$ was included in the calculation of the lattice thermal conductivity by considering only the effect of the different mass. The disorder in either the Petrov or Kooi structures is thus accounted for by adding a rate of elastic phonon scattering from isotopic impuri-

ties according to Ref. 30 (Eqs. 9 and 10 in Ref. 23). The presence of vacancies in the Ge/Sb sublattice was also included as an isotope impurity scattering with a mass change $\Delta M = 3M$ where M is the mass of the atom removed according to Ratsifaritana and Klemens³¹. The reliability of this approximation was validated for GeTe by means of non-equilibrium molecular dynamics simulations³² as discussed later on.

III. RESULTS

A. GeTe

At normal conditions, GeTe crystallizes in the trigonal ferroelectric phase (space group $R\bar{3}m$)³³. This structure, with two atoms per unit cell, can be viewed as a distorted rocksalt geometry with an elongation of the cube diagonal along the [111] direction and an off-center displacement of the inner Te atom along the [111] direction giving rise to a 3+3 coordination of Ge with three short stronger bonds (2.84 Å) and three long weaker bonds (3.17 Å). In the conventional hexagonal unit cell of the trigonal phase, the structure can be also seen as an arrangement of GeTe bilayers along the c direction with shorter intrabilayer bonds and weaker interbilayers bonds (cf. Fig. 1). The trigonal phase transforms experimentally into the cubic paraelectric phase (space group $Fm\bar{3}m$) above the Curie temperature of 705 K³⁴.

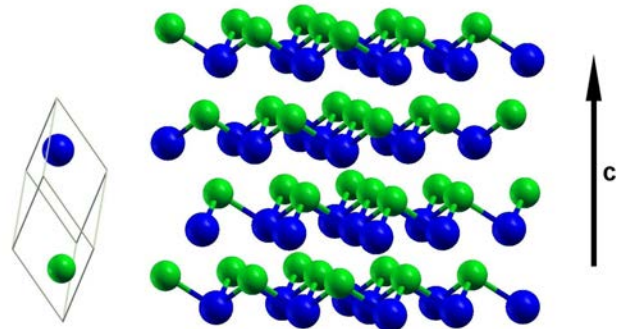


FIG. 1. Geometry of the GeTe crystal seen as a stacking of bilayers along the c axis of the conventional unit cell with the three short intrabilayers bonds and three long interbilayers bonds. Green spheres denote Ge atoms and blue spheres denote Te atoms.

The structural parameters of the trigonal phase consist of the lattice parameter a , the trigonal angle α , and the internal parameter x that assigns the positions of the two atoms in the unit cell, namely, Ge at (x, x, x) and Te at $(-x, -x, -x)$ ³³. The theoretical structural parameters optimized at zero temperature with the PBE functional with or without vdW corrections are compared in Table I with the LDA results and the experimental data. The Brillouin Zone (BZ) integration for the self-consistent electron density was performed over a $12 \times 12 \times 12$ MP mesh.

The equilibrium volume obtained with the PBE functional is very close to experiments while it is somehow underestimated with the LDA functional and the PBE functional plus vdW corrections.

Structural parameters	PBE	PBE +vdW	LDA	Exp.
a (Å)	4.33	4.22	4.23	4.31
α	58.14°	58.18°	58.79°	57.9°
Unit Cell Volume (Å ³)	54.98	51.75	52.00	53.88
x	0.2358	0.2380	0.2384	0.2366
Short, long bonds (Å)	2.85	2.82	2.83	2.84
	3.21	3.11	3.11	3.17

TABLE I. Structural parameters of the trigonal phase of crystalline GeTe computed within DFT with the LDA functional, the PBE functional with and without vdW interactions according to Grimme²⁶ and from experimental data³³. The length of short and long bonds are also given.

The ideal GeTe crystal is a narrow gap semiconductor with a DFT-PBE band gap of 0.45 eV. It turns into a p-type degenerate semiconductor because of defects in stoichiometry, in the form of Ge vacancies, which induce the formation of holes in the valence band³⁵. Hole concentrations are typically higher than 10^{19} holes/cm³ in native p-type doped GeTe³⁶. Higher hole concentration of $1.6 \cdot 10^{21}$ holes/cm³ which corresponds to a vacancy content of about 4.3 *atom%* in the Ge sublattice (two holes per Ge vacancy) was also reported²⁷.

In the calculation of phonon dispersion relations we considered the presence of holes at the lower content of $8 \cdot 10^{19}$ holes/cm³ measured in Ref. 36, but at first we did not consider the presence of the companion Ge vacancies. We relaxed the atom positions by keeping the lattice parameters fixed at the values of the ideal crystal which leads to a very small shift of the internal coordinate x to 0.2359 (for the PBE functional, cf. Table I). The Ge vacancies, present in the real crystal but lacking in our models of the p-type compound, are actually expected to affect the lattice parameters, as much as the holes in the valence bands do.

Phonons have been computed for the different functionals at the theoretical lattice parameters and for the LDA functional at the experimental lattice parameter as well.

The results for the PBE functional at the theoretical lattice parameter and, for LDA functional, at the experimental lattice parameters (close to the PBE ones) are compared in Fig. 2. The effect of holes on the phonon dispersions has been discussed in our previous work (with the PBE functional)³² and in Ref. 27 (with the LDA functional) to which we refer to for further details. Different functionals yield very similar results once the calculations are performed with similar lattice pa-

rameters as it is the case for PBE and LDA phonons at the experimental lattice parameters. The same is true for PBE+vdW and LDA results at the theoretical lattice parameters. Conversely sizable differences are observed between the phonon dispersions computed with LDA at the theoretical and experimental lattice parameters and between the PBE and PBE+vdW phonons again due to a large change in the corresponding equilibrium volumes. All phonon dispersion relations have been obtained by Fourier interpolating the dynamical matrix computed in a 6x6x6 MP grid in the BZ.

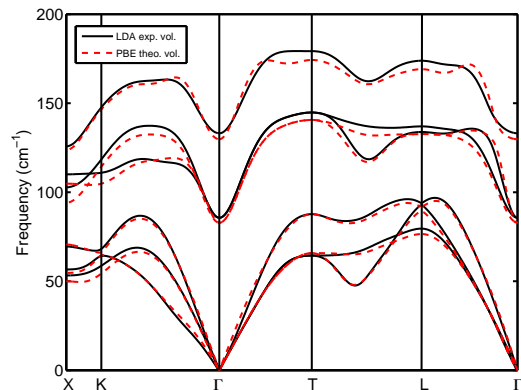


FIG. 2. Phonon dispersion relations of GeTe from PBE calculations at the theoretical equilibrium lattice parameters and from LDA calculations at the experimental lattice parameters (cf. Table I).

We then computed the lattice thermal conductivity for the ideal crystal at first without the effects of vacancies. Anharmonic forces have been computed on a 4x4x4 \mathbf{q} -point phonon grid on the BZ, Fourier interpolated with a finer 15x15x15 mesh for the BTE solution. Convergence was checked with a 25x25x25 grid. Phonon energies have been broadened with a Gaussian function with smearing of 2 cm⁻¹ for energy conservation in three-phonon scattering processes. The anharmonic force constants were computed only with the LDA functional by optimizing the internal geometry with the lattice parameters fixed to the values used in the corresponding calculations of harmonic phonons.

The resulting lattice thermal conductivity at 300 K computed with the exact variational solution of the BTE and PBE phonons along the z direction, parallel to the c axis in the hexagonal notation (cf. Fig. 1), is $\kappa_z = 2.00 \text{ W m}^{-1} \text{ K}^{-1}$ while the lattice thermal conductivity in the xy plane parallel to the GeTe bilayers (cf. Fig. 1) is $\kappa_x = 2.90 \text{ W m}^{-1} \text{ K}^{-1}$. For a polycrystalline sample the calculated average thermal conductivity is $\kappa_{av} = \frac{2}{3}\kappa_x + \frac{1}{3}\kappa_z = 2.6 \text{ W m}^{-1} \text{ K}^{-1}$, which is an upper limit, as it neglects the effects of defects (vacancies in particular) and grain boundary scattering. κ_{av} is comparable, although slightly larger, than the experimental value of $2.35 \pm 0.53 \text{ W m}^{-1} \text{ K}^{-1}$ of Ref. 10. Including the Grimme's van der Waals interaction in the phonons

calculation at the theoretical lattice parameters leads to a slightly higher thermal conductivities of $\kappa_z=2.30$ W m⁻¹ K⁻¹, $\kappa_x=3.38$ W m⁻¹ K⁻¹ and $\kappa_{av}=3.02$ W m⁻¹ K⁻¹. By using the LDA functional for both the harmonic and anharmonic force constants at the experimental lattice parameters one obtains an even larger lattice thermal conductivities of $\kappa_z=2.37$ W m⁻¹ K⁻¹, $\kappa_x=3.62$ W m⁻¹ K⁻¹ and $\kappa_{av}=3.20$ W m⁻¹ K⁻¹.

Using the equilibrium Boltzmann distribution of phonons instead of the quantum Bose-Einstein distribution has no effect on the lattice thermal conductivity at 300 K (within the figures given here) due to the low Debye temperature (180 K). For the same reason the lattice thermal conductivities computed within the SMA are only slightly lower than the values obtained from the full solution of the BTE.

The lattice thermal conductivity within SMA is given by²³

$$\kappa_x = \frac{1}{N_{\mathbf{q}}V_o} \sum_{\mathbf{q},j} C_{\mathbf{q},j} v_{\mathbf{q},j}^2 \tau_{\mathbf{q},j} \quad (1)$$

where the sum runs over the band index j and the $N_{\mathbf{q}}$ points in the BZ, $v_{\mathbf{q},j}$ is the group velocity along a generic coordinate x for band j at point \mathbf{q} , $C_{\mathbf{q},j}$ is the contribution to the specific heat of the (\mathbf{q}, j) -phonon with frequency $\omega_{\mathbf{q},j}$ obtained from the derivative of the Bose-Einstein function f_{BE} with respect to temperature as $\hbar\omega_{\mathbf{q},j}\partial f_{BE}(\omega_{\mathbf{q},j})/\partial T$, V_o is the unit cell volume, and $\tau_{\mathbf{q},j}$ is phonon lifetime obtained in turn from anharmonic force constants as discussed in Ref. 23 (cf. Eq. B1 therein). This approximation, when applicable, provides a more straightforward physical insight of the system, allowing to account separately for each contributing factor to the thermal conductivity that appears in Eq.1, and will be used with this purpose in the present paper after checking its validity by comparison with the exact BTE solution.

A summary of the resulting thermal conductivity computed with the different functionals and the comparison among the exact solution of the BTE and the SMA approximation are reported in in Tab.II.

	Exact			SMA		
	κ_z	κ_x	κ_{av}	κ_z	κ_x	κ_{av}
PBE	2.00	2.90	2.60	1.80	2.61	2.34
PBE+vdW	2.30	3.38	3.02	1.92	2.91	2.58
LDA	2.37	3.62	3.20	2.00	3.10	2.70

TABLE II. Lattice thermal conductivity of ideal trigonal GeTe at 300 K along the c axis in the hexagonal notation (κ_z , cf. Fig. 1) in the perpendicular plane (κ_x) and their average for a polycrystalline sample (κ_{av} , see text), computed with the exact variational solution of the BTE and within the SMA.

The cumulative lattice thermal conductivity within the SMA of ideal trigonal GeTe as a function of phonons fre-

quency is shown in Fig. 3 along with group velocities, phonon lifetimes and mean free paths averaged over a small energy window of 2 cm⁻¹. The anharmonic broadening of the phonon branches computed as the inverse lifetime (Eq. 6 in Ref. 22) within the SMA are also reported in Fig. 4. Another visualization of the anharmonic broadening is obtained by plotting the spectral function multiplied by the phonon frequency $\omega \cdot \sigma(\omega, \mathbf{q})$ shown in Fig. 5 where $\sigma(\omega, \mathbf{q})$ defined by³⁷

$$\sigma(\mathbf{q}, \omega) = \sum_j \frac{2\omega_{\mathbf{q},j}\tau_{\mathbf{q},j}^{-1}}{[\hbar^2(\omega^2 - \omega_{\mathbf{q},j}^2)]^2 + 4\hbar^2\omega_{\mathbf{q},j}^2\tau_{\mathbf{q},j}^{-2}} \quad (2)$$

Comparison of Fig. 3a and Fig. 4 shows that the thermal conductivity is mostly due to acoustic phonons even at 300 K because of both low group velocities and lifetimes of optical phonons. All the data in Figs. 3-7 refer to LDA calculations at the experimental lattice parameters.

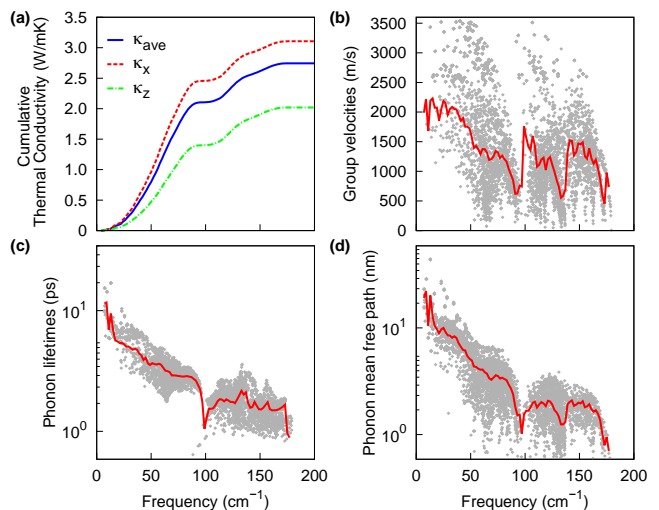


FIG. 3. (a) Cumulative lattice thermal conductivities within the SMA (see text) along the c axis in the hexagonal notation (κ_z , cf. Fig. 1) in the perpendicular plane (κ_x) and their average for a polycrystalline sample (κ_{av} , see text), (b) group velocities, (c) phonon lifetimes, and (d) mean free paths averaged over a small energy window of 2 cm⁻¹ shown a function of phonon frequencies in the ideal GeTe crystal (no vacancies) at 300 K. The data refer to LDA calculations at the experimental lattice parameters.

We then included the effects of vacancies in the Ge sublattice on the thermal conductivity by adding a rate of elastic scattering as due to isotopic defects in the BTE (cf. Sec. II). We considered two limiting vacancy contents of 0.2 *atom%* on the Ge sublattice corresponding to the hole concentration of $8 \cdot 10^{19}$ holes/cm³ studied experimentally in Ref. 36, and of 3 *atom%* that corresponds to a hole concentration of $1.1 \cdot 10^{21}$ holes/cm³ close to that studied experimentally in Ref. 27. The lattice thermal conductivity (LDA phonons at the experimental lattice parameters and exact solution of the BTE) turns into

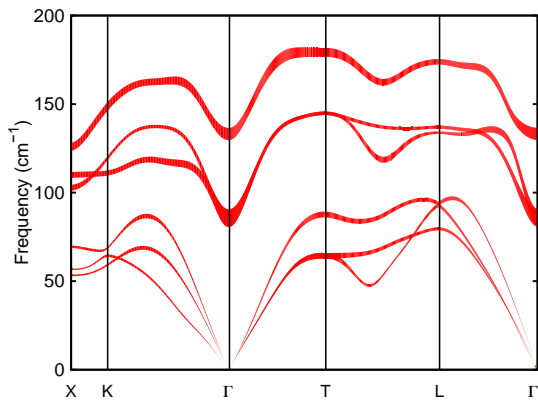


FIG. 4. Phonon dispersion relations of GeTe from LDA calculations at the experimental lattice parameters (cf. Table I). The thickness of the curves corresponds to the anharmonic broadening computed as the inverse lifetime within the SMA.

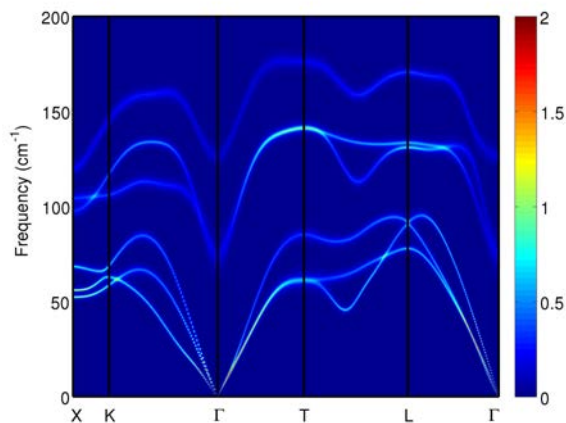


FIG. 5. Spectral function $\omega \cdot \sigma(\mathbf{q}, \omega)$ (cf. Eq. 2) of GeTe from LDA calculations at the experimental lattice parameters and only anharmonic broadening.

$\kappa_z=2.0 \text{ W m}^{-1} \text{ K}^{-1}$, $\kappa_x=3.0 \text{ W m}^{-1} \text{ K}^{-1}$ and $\kappa_{av}=2.7 \text{ W m}^{-1} \text{ K}^{-1}$ for the low vacancy content or $\kappa_z=0.9 \text{ W m}^{-1} \text{ K}^{-1}$, $\kappa_x=1.4 \text{ W m}^{-1} \text{ K}^{-1}$ and $\kappa_{av}=1.2 \text{ W m}^{-1} \text{ K}^{-1}$ for the higher vacancy concentration to be compared with the values for the ideal GeTe of $\kappa_z=2.37 \text{ W m}^{-1} \text{ K}^{-1}$, $\kappa_x=3.62 \text{ W m}^{-1} \text{ K}^{-1}$ and $\kappa_{av}=3.20 \text{ W m}^{-1} \text{ K}^{-1}$ as given above. Even a small amount of Ge vacancies has thus a dramatic effect on the lattice thermal conductivity of GeTe which can be more than halved for a 3 *atom%* in agreement with the experimental data in Ref. 15.

We remark that the effect of vacancies on the thermal conductivity has been actually introduced perturbatively as isotopic defects according to Ref. 31. To assess the reliability of this approximation, we have performed non-equilibrium molecular dynamics (NEMD) simulations by using a highly transferable interatomic potential for GeTe obtained by fitting a large database of DFT-PBE energies with a Neural Network Method³⁹. The reliability

of the classical approximation for phonons population at 300 K in GeTe, implicit in NEMD, has been demonstrated above. The NEMD simulations reported in Ref. 32 yields an average lattice thermal conductivity κ_{av} of $3.2 \text{ W m}^{-1} \text{ K}^{-1}$ or $1.4 \text{ W m}^{-1} \text{ K}^{-1}$ for the ideal crystal or with 3 *atom%* of Ge vacancies. The reduction of the thermal conductivity due to vacancies is quantitatively similar to the results obtained from BTE which yields $3.2 \text{ W m}^{-1} \text{ K}^{-1}$ or $1.2 \text{ W m}^{-1} \text{ K}^{-1}$ for the ideal and defective (3 % of vacancies) crystal (LDA phonons at the experimental lattice parameters). The good agreement between the NEMD and BTE results assess the reliability of the approximation used to deal with Ge vacancies in the solution of the BTE. The cumulative lattice thermal conductivity and average phonon mean free path within the SMA is shown in Fig. 6 as a function of phonons frequency for trigonal GeTe with 3 *atom%* of Ge vacancies. These results have to be compared with the corresponding data for ideal GeTe in Fig. 3.

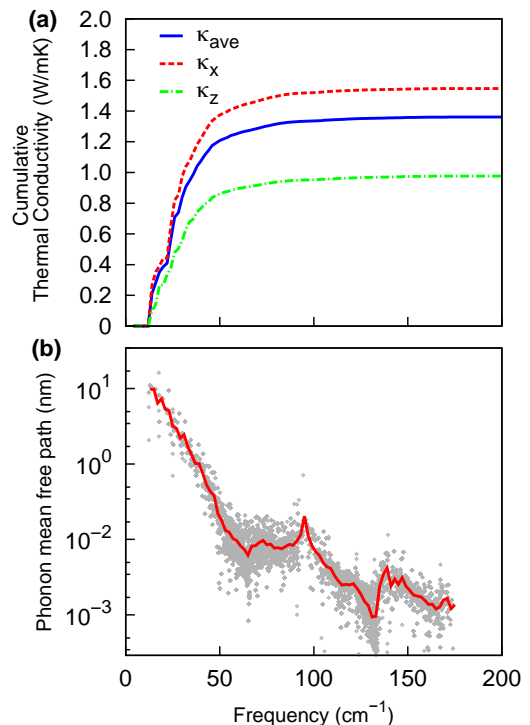


FIG. 6. (a) Cumulative lattice thermal conductivities within the SMA (see text) along the *c* axis in the hexagonal notation (κ_z , cf. Fig. 1) in the perpendicular plane (κ_x) and their average for a polycrystalline sample (κ_{av} , see text), and (b) mean free paths averaged over a small window of 2^{-1} as a function of phonon frequencies for GeTe with 3 *atom%* of Ge vacancies at 300 K. The data refer to LDA calculations at the experimental lattice parameters.

We further remark that in the presence of holes in the valence bands the phonon lifetimes can be reduced also by electron-phonon scattering processes. These effects are, however, negligible in GeTe at the doping levels discussed above. To estimate the reduction of thermal con-

ductivity due to electron-phonon scattering we removed from the calculation of κ the contribution of all phonons with wavevector q smaller than twice the larger wavevector on the Fermi surface. This would correspond to a large overestimation of the effects of the electron-phonon coupling that, nevertheless, leads to a slight reduction of the thermal conductivities to $\kappa_z=2.2 \text{ W m}^{-1} \text{ K}^{-1}$ and $\kappa_x=3.1 \text{ W m}^{-1} \text{ K}^{-1}$.

Finally, we calculated the temperature dependence of the thermal conductivity in GeTe with a 3% vacancies as reported in Fig 7.

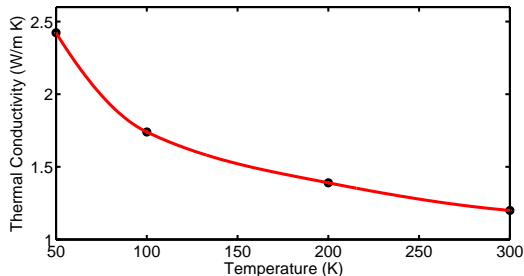


FIG. 7. Temperature dependence of thermal conductivity of polycrystalline GeTe with 3% of Ge vacancies. The data refer to LDA phonons at the experimental lattice parameters.

B. Sb_2Te_3

Crystalline Sb_2Te_3 has a rhombohedral geometry ($R\bar{3}m$ space group (D_{3d}^5)) with five atoms per unit cell³⁸. The crystal structure can be better visualized in the conventional hexagonal supercell with three formula units (Fig. 8). In the hexagonal cell we recognize three slabs, each formed by five hexagonal layers stacked along c in the sequence Te-Sb-Te-Sb-Te, each layer containing a single atom in the unit cell. The weak Te-Te bonds, 3.736 Å long³⁸, connecting adjacent slabs are not shown in Fig. 8 to emphasize the presence of Sb_2Te_3 structural units. The three atoms independent by symmetry are at crystallographic positions $\text{Te1} = (0, 0, 0)$, $\text{Te2} = (0, 0, x)$ and $\text{Sb} = (0, 0, y)$ (Fig. 8).

We computed the phonon dispersion relation of Sb_2Te_3 with the PBE functional in our previous work⁴⁰. Here, we consider the PBE functional supplemented by the vdW corrections²⁶ to better reproduce the weak Te-Te interaction. The equilibrium structural parameters obtained with PBE and PBE+vdW functionals are compared in Table III with the experimental data³⁸. Integration of the BZ for the self-consistent solution of the Kohn-Sham equation is performed over a 6x6x6 MP mesh.

Experimentally this compound is a degenerate p-type semiconductor with a hole concentration of about $1.0 \cdot 10^{20} \text{ holes/cm}^3$ possibly due to an Sb excess substituting Te¹¹. As for the case of GeTe, we introduced holes in the valence bands compensated by a uniform negative background to ensure charge neutrality. The internal struc-

ture has been optimized by fixing the lattice parameters to those obtained without holes. Phonon dispersion relations have been obtained by Fourier transforming the dynamical matrix computed on a 6x6x6 MP grid in the BZ.

The dispersion curves computed with PBE+vdW functionals at the theoretical equilibrium parameters are reported in Fig. 9 together with the available experimental data from neutron inelastic scattering⁴¹.

Anharmonic force constants have been computed following the same scheme used for GeTe and discussed in the previous section. A 4x4x4 q-point grid has been used. Fourier interpolation has been made over a 15x15x15 grid with a smearing of 2 cm^{-1} for energy conservation.

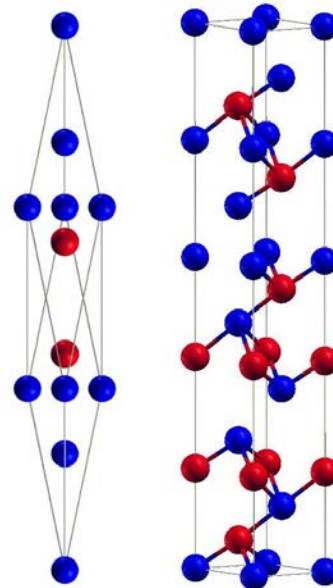


FIG. 8. Structure of Sb_2Te_3 in the unit rhombohedral cell and conventional hexagonal supercell (three formula units). Blue and red spheres denote Te and Sb atoms.

Structural parameters	PBE	PBE+vdW	Exp.
a (Å)	4.316	4.219	4.264
c (Å)	31.037	30.692	30.458
x	0.785	0.786	0.787
y	0.397	0.397	0.399

TABLE III. Structural parameters of crystalline Sb_2Te_3 from DFT calculations with the PBE or PBE+vdW functionals (see text) compared with the experimental data from Ref. 38.

The resulting lattice thermal conductivities at 300 K computed with PBE+vdW phonons and solving exactly the BTE are $\kappa_z=0.8 \text{ W m}^{-1} \text{ K}^{-1}$, $\kappa_x=2.0 \text{ W m}^{-1} \text{ K}^{-1}$, and $\kappa_{av}=1.6 \text{ W m}^{-1} \text{ K}^{-1}$ which compares well with

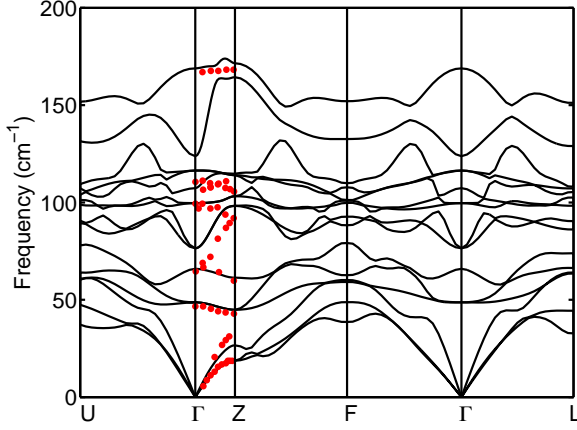


FIG. 9. Phonon dispersion relations of Sb_2Te_3 from PBE+vdW calculations. The dots are experimental data from neutron inelastic scattering measurements at room temperature⁴¹.

the experimental value of $\kappa_{av} = 1.3 \text{ W m}^{-1} \text{ K}^{-1}$ of Ref. 11 or $1.8 \text{ W m}^{-1} \text{ K}^{-1}$ of Ref. 16. Also in this case the difference between the exact BTE solution and the SMA is rather small with a SMA thermal conductivity of $\kappa_z = 0.78 \text{ W m}^{-1} \text{ K}^{-1}$, $\kappa_x = 1.9 \text{ W m}^{-1} \text{ K}^{-1}$.

In our model of Sb_2Te_3 the sublattice is ordered, but we expect a concentration of about 0.26 % of vacancy in the Sb sublattice (fraction of Sb sites empty) due to a hole concentration of $10^{20}/\text{cm}^{211}$. This small vacancy content could bring the slightly overestimated theoretical thermal conductivity to a better agreement with experiments. We remark that the experimental lattice thermal conductivities are always obtained from the total thermal conductivity and the subtraction of the electronic contribution by applying the Wiedemann-Franz law.

The thermal conductivity is strongly anisotropic due to the presence of weak Te-Te bonds between adjacent quintuple layers. The cumulative lattice thermal conductivity within the SMA of Sb_2Te_3 as a function of phonons frequency is shown in Fig. 10 along with average group velocities, phonon lifetimes and mean free paths. The contribution of optical modes to the thermal conductivity is marginally more important for Sb_2Te_3 than for the GeTe reaching here a contribution of 35 %.

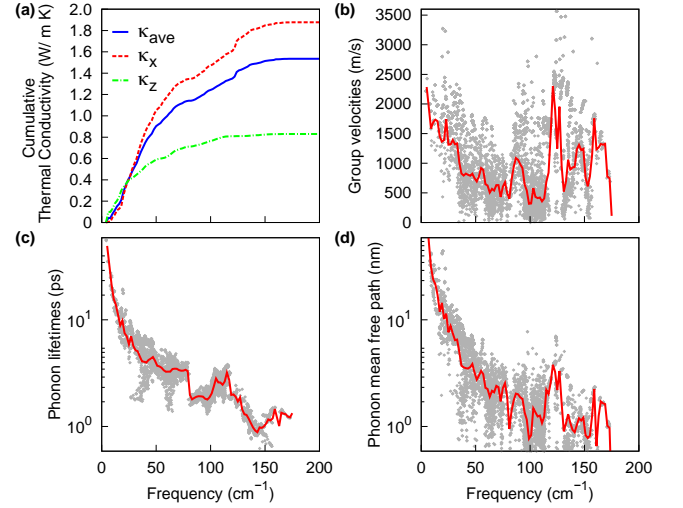


FIG. 10. (a) Cumulative lattice thermal conductivities within the SMA (see text) along the c axis in the hexagonal notation (κ_z , cf. Fig. 1) in the perpendicular plane (κ_x) and their average for a polycrystalline sample (κ_{av} , see text), (b) group velocities, (c) phonon lifetimes, and (d) mean free paths averaged over a small window of 2 cm^{-1} as a function of phonon frequencies in Sb_2Te_3 crystal at 300 K.

C. $\text{Ge}_2\text{Sb}_2\text{Te}_5$

The hexagonal phase of $\text{Ge}_2\text{Sb}_2\text{Te}_5$ has $P\bar{3}m1$ symmetry and nine atoms per unit cell in nine layers stacked along the c axis. Two different stacking sequences have been proposed, namely the ordered stacking Te-Sb-Te-Ge-Te-Ge-Te-Sb-Te-Te-Sb¹⁷ shown in Fig. 11 (stacking A in Ref. 42 and hereafter) and the ordered stacking Te-Ge-Te-Sb-Te-Sb-Te-Ge-Te-Te-Ge¹⁸ (stacking B in Ref. 42 and hereafter). As already mentioned, recent diffraction measurements suggested, however, a disordered phase with Sb and Ge randomly occupying the same layers¹⁹ (stacking C in Ref. 42 and hereafter) which is also confirmed by transmission electron microscopy imaging of GST nanowires²⁰. The structure can be seen as a stacking of $\text{Ge}_2\text{Sb}_2\text{Te}_5$ quintuple layers with weak Te-Te bonds between adjacent layers.

In a previous work⁴² we optimized the geometry of $\text{Ge}_2\text{Sb}_2\text{Te}_5$ in stackings A and B within DFT-PBE. We also modeled the disordered phase C by doubling the unit cell along the b axis and putting one Ge and one Sb atom on each Ge/Sb layer (18-atom supercell). The geometry chosen for stacking C corresponds to the best quasi-random structure compatible with an 18-atom supercell⁴³. Stacking A is lower in energy than stacking B (by 19 meV/atom). Stacking C is only marginally higher in energy than stacking A, actually within the free energy contribution expected for configurational disorder, and it is even marginally lower in energy than stacking A if the hybrid B3PW functional⁴⁴ is used. The crystal structure of $\text{Ge}_2\text{Sb}_2\text{Te}_5$ in stacking A was optimized in Ref. 42 by constraining the $P\bar{3}m1$ crystal symmetry.

Stacking			
	Kooi	Petrov	Exp.
Energy (meV/atom)	0 (0)	16 (19)	
Cell Parameters (Å)			
a	4.191 (4.28)	4.178 (4.25)	4.225
c	17.062 (17.31)	17.41 (17.74)	17.239

TABLE IV. Relative energies (meV/atom) and theoretical equilibrium lattice parameters (Å) for stacking A (Kooi) and B (Petrov) optimized with the PBE+vdW functional. Data without vdW corrections are reported in parenthesis. The experimental data are from Ref. 19

This procedure was chosen because of the presence of an unstable optical phonon at the Γ -point⁴². This instability is actually removed by adding a vdW interaction according to Grimme²⁶ as discussed in Ref. 45. Therefore, the thermal conductivity has been computed here using the PBE functional supplemented by the vdW interaction of Ref. 26. The equilibrium theoretical lattice parameters of $\text{Ge}_2\text{Sb}_2\text{Te}_5$ in stacking A and B obtained with the PBE functional with and without vdW corrections are compared with experimental data in Table IV. The BZ was sampled over a $8 \times 8 \times 8$ MP mesh for the self-consistent electron density. GST is a degenerate p-type semiconductor as well with a hole density of about $2.73 \cdot 10^{20}$ holes/cm³⁴⁶. We consistently introduced holes ($3 \cdot 10^{20}$ holes/cm³) compensated by a uniform background. The internal structure has been relaxed by fixing the lattice parameters to the values obtained without holes with negligible changes.

Phonon dispersion relations have been obtained by Fourier transforming the dynamical matrix computed on a $4 \times 4 \times 4$ MP grid in the BZ. Phonon dispersion relations are shown in Fig. 12 for the two stackings with and without vdW correction.

Anharmonic force constants have been computed following the same scheme used for GeTe and discussed in the previous sections. A $4 \times 4 \times 1$ q-point grid has been used. Fourier interpolation has been made over a $20 \times 20 \times 7$ grid with a smearing of 2 cm^{-1} for energy conservation.

The thermal conductivities at 300 K for the ordered $\text{Ge}_2\text{Sb}_2\text{Te}_5$ crystal in stacking A and B obtained from the full solution of the BTE with the PBE+vdW functional are reported in Table V compared with the SMA result which is lower by less than 5 % with respect to the value obtained from the full solution of the BTE. The average thermal conductivity of about $1.6\text{-}1.2 \text{ W m}^{-1} \text{ K}^{-1}$ is sizably larger than the experimental value of $0.45 \text{ W m}^{-1} \text{ K}^{-1}$ reported in Ref.9.

The spectral function (Eq. 2) of GST in stacking A and B and including only anharmonic lifetimes are shown in Fig. 13. The cumulative lattice thermal conductivity within the SMA of $\text{Ge}_2\text{Sb}_2\text{Te}_5$ as a function of phonons frequency is shown in the side columns of Fig. 14 for stacking A and B along with group velocities, phonon

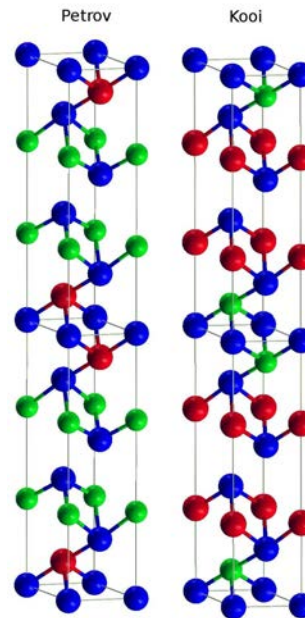


FIG. 11. Structure of $\text{Ge}_2\text{Sb}_2\text{Te}_5$ in the hexagonal cell in stacking A (Kooi) and B (Petrov). Two formula units along the c axis, and period replica of atoms at the edges of the hexagonal cell in the ab plane are shown. Atoms independent by symmetry are labeled. In stacking A and B, the positions of Ge and Sb atoms are interchanged. The weak TeTe bonds (3.7 \AA long) connecting adjacent slabs are not shown to emphasize the presence of $\text{Ge}_2\text{Sb}_2\text{Te}_5$ stacks. Blue, green and red spheres denote Te, Ge and Sb atoms.

	Exact			SMA		
	κ_z	κ_x	κ_{av}	κ_z	κ_x	κ_{av}
Kooi	0.34	1.59	1.20	0.34	1.51	1.12
Petrov	0.59	2.10	1.60	0.58	2.00	1.53

TABLE V. Lattice thermal conductivity of hexagonal $\text{Ge}_2\text{Sb}_2\text{Te}_5$ at 300 K along the c axis in the hexagonal notation (κ_z , cf. Fig. 11) in the perpendicular plane (κ_x) and their average for a polycrystalline sample (κ_{av} , see text). Both stacking A (Kooi) and B (Petrov) are considered. The thermal conductivity are computed for the perfect crystals using the exact variational solution of the BTE and within the SMA.

lifetimes and mean free paths averaged over a small energy window of 2 cm^{-1} .

We then introduced in the BTE the scattering due to vacancies in either the Sb or Ge sublattice with a concentration assigned by the holes density of $3 \cdot 10^{20}$ holes/cm³ close to the value measured by the Hall effect⁴⁶. This holes density corresponds to either 1.8 atom% vacancies in the Ge sublattice (two holes per vacancy involving only electrons from p orbitals) or to 1.25 atom% vacancies in the Sb sublattice (three holes per vacancy). The average thermal conductivity is reduced to about $0.8\text{-}1.1 \text{ W m}^{-1} \text{ K}^{-1}$ (Table VI) which is still much higher than the experimental value. By increasing the vacancy concen-

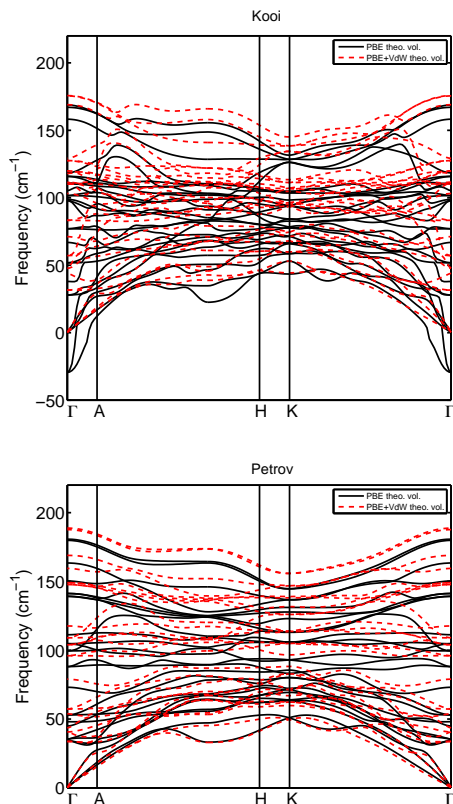


FIG. 12. Phonon dispersion relations of $\text{Ge}_2\text{Sb}_2\text{Te}_5$ for stacking A (Kooi) and B (Petrov) stackings from PBE and PBE+vdW calculations.

tration up to 3 atom% in the Ge sublattice the average thermal conductivity is further reduced to $0.64\text{-}0.86 \text{ W m}^{-1} \text{ K}^{-1}$.

To better model the experimental conditions, we have then introduced disorder in the Ge/Sb sublattice by adding an isotopic phonon scattering rate in the BTE (see Sec. II). By considering a full Ge/Sb mass mixing and neglecting Ge/Sb vacancies the average thermal conductivity is sizably reduced to $0.61\text{-}0.76 \text{ W m}^{-1} \text{ K}^{-1}$ (cf. Table VI). By further adding on top of Ge/Sb disorder the scattering due to 1.8 atom% Ge vacancies or 1.25 atom% Sb vacancies, the average thermal conductivity is further reduced to $0.43\text{-}0.58 \text{ W m}^{-1} \text{ K}^{-1}$ or $0.28\text{-}0.42 \text{ W m}^{-1} \text{ K}^{-1}$ (cf. Table VI).

The cumulative lattice thermal conductivity within the SMA of $\text{Ge}_2\text{Sb}_2\text{Te}_5$ as a function of phonons frequency is shown in the central column Fig. 14 for stacking B by including Sb/Ge disorder (Matsunaga model) and vacancies in the Sb sublattice. Group velocities, phonon lifetimes and mean free paths averaged over a small energy window of 2 cm^{-1} are also shown in the same figure. The temperature dependence of the thermal conductivity for this latter system averaged over the three cartesian directions is shown in Fig. 15.

From Figs. 13-14 it is clear that the acoustic phonons mostly contribute to the thermal conductivity at 300 K,

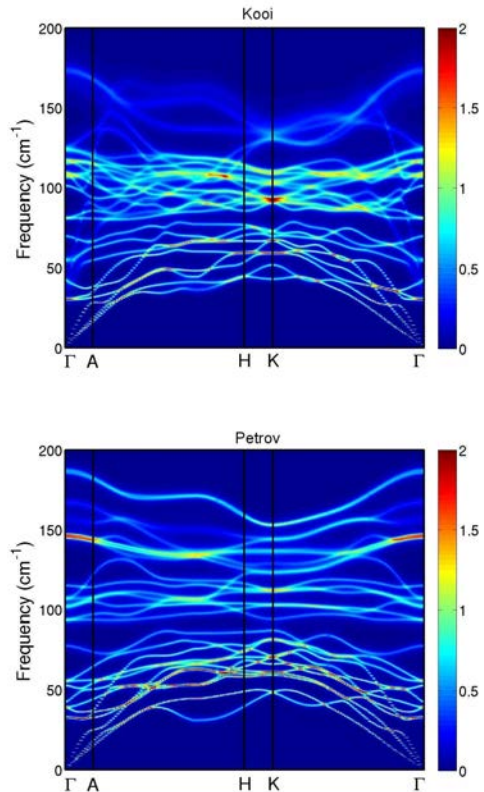


FIG. 13. Spectral function $\omega \cdot \sigma(\mathbf{q}, \omega)$ (cf. Eq. 2) of GST in the stacking A (Kooi) and B (Petrov) with anharmonic broadening only.

with a small contribution from the lower energy optical modes and a negligible contribution from the high energy optical modes. In the disordered Matsunaga phase in particular, the whole lattice thermal conductivity originates from the acoustic modes with energy below 30 cm^{-1} .

Note that disordering the Kooi or Petrov structures with a 50-50 occupation by Sb and Ge in all layers leads to the same structure and thus in principles to the same lattice thermal conductivity. This is not the case for the results in Table IV because disorder has been introduced perturbatively. This approximation leads to a dependence of the final results on the choice of the ordered starting configuration. In the structural model proposed by Matsunaga, the disorder in the occupation of the Ge/Sb sites is actually not complete as the cationic lattice sites closer to the vdW gap are occupied by Sb in a fraction of 56 % (with a reversed proportion for the inner cationic sites). The uncertainties related to our perturbative approach to the disorder prevent us to assess such small deviations from a 50-50 occupation of the Sb/Ge sites on the basis of the calculated thermal conductivity. In spite of these uncertainties, it is clear that both vacancies and disorder are needed to achieve a good agreement between theoretical and experimental data (cd. Table VI). This result strongly suggests that the low thermal conductivity in the hexagonal phase of GST is actually an

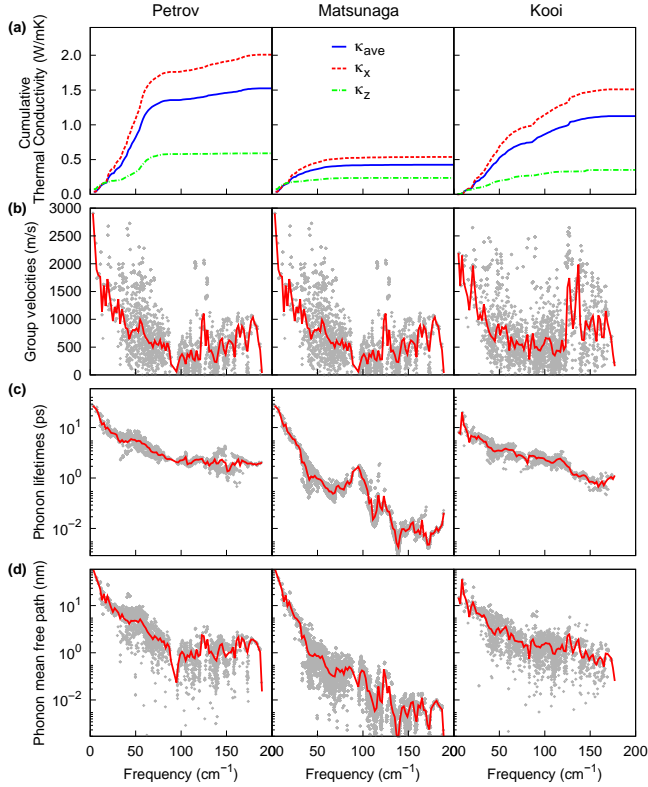


FIG. 14. (a) Cumulative lattice thermal conductivities within the SMA (see text) along the c axis in the hexagonal notation (κ_z , cf. Fig. 1) in the perpendicular plane (κ_x) and their average for a polycrystalline sample (κ_{av} , see text), (b) group velocities, (c) phonon lifetimes, and (d) mean free paths over a small energy window of 2 cm^{-1} as a function of phonon frequencies in $\text{Ge}_2\text{Sb}_2\text{Te}_5$ crystal at 300 K for stacking A (Kooi, left panels), B (Petrov, right panels) and for the disordered stacking according to Matsunaga (central panel) including vacancies (see text)

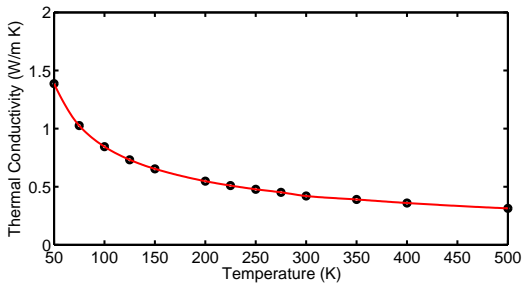


FIG. 15. Temperature dependence of thermal conductivity of polycrystalline GST with disorder in the Sb/Ge sublattice and including vacancies (see text).

indicator of the (Ge/Sb) sublattice disorder confirmed by recent experimental data from Z-resolved TEM in GST nanowires²⁰.

We remark that the thermal conductivity obtained from the solution of the BTE with the inclusion of disorder

	A (Kooi)			B (Petrov)		
	κ_z	κ_x	κ_{av}	κ_z	κ_x	κ_{av}
Ideal	0.34	1.59	1.20	0.59	2.10	1.60
1.8 % Ge vac	0.28	1.19	0.83	0.42	1.49	1.13
1.25 % Sb vac	0.25	1.10	0.82	0.47	1.50	1.16
Ge/Sb disorder	0.20	0.77	0.61	0.30	0.99	0.76
Ge/Sb + Ge vac	0.16	0.56	0.43	0.25	0.75	0.58
Ge/Sb + Sb vac	0.11	0.37	0.28	0.23	0.51	0.42

TABLE VI. Lattice thermal conductivity of hexagonal $\text{Ge}_2\text{Sb}_2\text{Te}_5$ at 300 K along the c axis in the hexagonal notation (κ_z , cf. Fig. 11) in the perpendicular plane (κ_x) and their average for a polycrystalline sample (κ_{av} , see text). Both stacking A (Kooi) and B (Petrov) are considered. The thermal conductivity are computed for the perfect crystals (ideal) for a crystal with 1.8 *atom*% of Ge vacancies (1.8 % Ge vac, see text), for 1.25 *atom*% of Sb vacancies (1.25 % Sb vac, see text), for a complete disorder in the Ge/Sb sublattice with no vacancies (Ge/Sb disorder), and finally with both disorder in the Ge/Sb and a content of Ge vacancies (Ge/Sb + Ge vac) or Sb vacancies (Ge/Sb + Sb vac) as given above. All the results refer to the exact BTE solution however the differences between exact and SMA results are marginal. Data are given in $\text{W m}^{-1} \text{K}^{-1}$. The experimental lattice thermal conductivity is $0.45 \text{ W m}^{-1} \text{K}^{-1}$.

der in the Sb/Ge sublattice and vacancies in $\text{Ge}_2\text{Sb}_2\text{Te}_5$. ($0.42 \text{ W m}^{-1} \text{K}^{-1}$ in Table VI) is very close to the minimum thermal conductivity obtained from the theoretical average transverse and longitudinal sound velocity (v_L , v_T) and atomic density n_a according to Cahill⁴⁸ and valid above the Debye temperature as given by

$$\kappa_{min} = \frac{1}{2} \left(\frac{\pi n_a^2}{6} \right)^{\frac{1}{3}} (v_L + 2v_T) k_B \quad (3)$$

where k_B is the Boltzmann constant. By plugging in Eq. 3 the sound velocities averaged over the BZ $v_L=3120 \text{ m/s}$ and $v_T=1950 \text{ m/s}$ one finds $\kappa_{min}=0.43 \text{ W m}^{-1} \text{K}^{-1}$ close to the full DFT solution and to the experimental value of $0.45 \text{ W m}^{-1} \text{K}^{-1}$ as already observed in Refs. 9 and 49. This result raises overall concern on the applicability of the BTE itself in the presence of such a strong phonon scattering due to disorder. However, as we can see in Fig. 14, disorder does not affect the phonon mean free path in the same manner for all frequencies. The disorder actually suppresses the contribution to the thermal conductivity of phonons with frequency above 50 cm^{-1} which give instead an important contribution to the thermal conductivity of the ideal crystal. On the other hand phonons with frequency below 30 cm^{-1} that mostly contribute to the thermal conductivity of the disordered crystal still show a mean free path of several nm which seems consistent with the use of a BTE approach.

IV. CONCLUSIONS

We have computed the lattice thermal conductivity of the phase change compound $\text{Ge}_2\text{Sb}_2\text{Te}_5$ in the hexagonal crystalline phase from the full solution of the linearized Boltzmann transport equation with phonons and phonon-phonon scattering rates computed within Density Functional Perturbation Theory. Due to the weak Te-Te bonds the lattice thermal conductivity is strongly anisotropic with a low conductivity along the c axis. However, scattering due to disorder in Sb/Ge sublattice has to be introduced to bring the thermal conductivity close to the value of $0.45 \text{ W m}^{-1} \text{ K}^{-1}$ measured experimentally. These results confirm the presence of disorder in the Sb/Ge sublattices emerged from most recent x-ray diffraction data¹⁹ and from transmission electron mi-

croscopy of nanowires²⁰. The same calculations on the GeTe trigonal crystal reveal that the presence of Ge vacancies, responsible for a degenerate p-type character, leads to the large variability of the bulk thermal conductivity measured experimentally for this compound. A similarly good agreement with experiments is obtained for the thermal conductivity of Sb_2Te_3 .

ACKNOWLEDGMENTS

MB acknowledges funding from the European Union Seventh Framework Programme FP7/2007-2013 under grant agreement No. 310339 and computational resources provided by Cineca (Casalecchio di Reno, Italy) through the ISCRA initiative. LP and FM acknowledge funding from DARI, dossier 2015097320.

-
- * corresponding authors: davide.campi@epfl.ch
- ¹ M. Wuttig and N. Yamada, *Nat. Mater.* **6**, 824 (2007).
 - ² A. Pirovano, A. L. Lacaita, A. Benvenuti, F. Pellizzer, and R. Bez, *IEEE Trans. Electron. Dev.* **51**, 452 (2004).
 - ³ A.L. Lacaita and D.J. Wouters, *Phys. Stat. Sol. A* **205**, 2281 (2008).
 - ⁴ D. Lencer, M. Salinga, and M. Wuttig, *Adv. Mat.* **23**, 2030 (2011).
 - ⁵ S. Raoux, W. Welnic, and D. Ielmini, *Chem. Rev.* **110**, 240 (2010).
 - ⁶ J. P. Reifenberg, D. L. Kencke, and K. E. Goodson, *IEEE Elec. Dev. Lett.* **29**, 1112 (2008).
 - ⁷ E. Bozorg-Grayeli, J. P. Reifenberg, M. Asheghi, H.-S. P. Wong, and K. E. Goodson, *Annual Review of Heat Transfer* **15**, 397 (2013).
 - ⁸ K. S. Siegert, F. R. L. Lange, E. R. Sittner, H. Volker, C. Schlockermann, T. Siegrist, and M. Wuttig, *Rep. Prog. Phys.* **78** 013001 (2015).
 - ⁹ J. Lee, E. Bozorg-Grayeli, S. B. Kim, M. Asheghi, P.H.-S. Wong, K. E. Goodson, *Appl. Phys. Lett.* **102**, 191911 (2013).
 - ¹⁰ R. Fallica, E. Varesi, L. Fumagalli, S. Spadoni, and M. Longo, *Physica Status Solidi RRL* **7**, 1107 (2013).
 - ¹¹ L. E. Shelimova, O. G. Karpinskii, P. P. Konstantinov, M. A. Kretova, E. S. Avilov, and V. S. Zemskov, *Inorg. Mat.* **37**, 421 (2001).
 - ¹² P. Nath and K. L. Chopra, *Phys. Rev. B* **10**, 3412 (1974).
 - ¹³ R. Lan, R. Endo, M. Kuwahara, Y. Kobayashi, and M. Susa, *J. Appl. Phys.* **112**, 053712 (2012).
 - ¹⁴ J. M. Yanez-Limon, J. Gonzalez-Hernandez, J. J. Alvarado-Gil, I. Delgadillo, and H. Vargas, *Phys. Rev. B* **52**, 16321 (1995).
 - ¹⁵ D. H. Damon, M. S. Lubell, and R. Mazelsky, *J. Phys. Chem. Solids* **28**, 520 (1967).
 - ¹⁶ K. Yokota and S. Katayama, *Jpn. J. Appl. Phys.* **12**, 1205 (1973).
 - ¹⁷ B. J. Kooi and T. M. J. De Hosson, *J. Appl. Phys.* **92**, 3584 (2002).
 - ¹⁸ I. I. Petrov, R. M. Imanov, and Z. G. Pinsker, *Sov. Phys. Crystallogr.* **13**, 339 (1968).
 - ¹⁹ T. Matsunaga, N. Yamada, and Y. Kubota, *Acta Cryst. B* **60**, 685 (2004).
 - ²⁰ E. Rotunno, L. Lazzarini, M. Longo, and V. Grillo, *Nanoscale* **5**, 1557 (2013).
 - ²¹ S. Baroni, S. de Gironcoli, and A. Dal Corso, *Rev. Mod. Phys.* **73**, 515 (2001).
 - ²² L. Paulatto, F. Mauri, and M. Lazzeri, *Phys. Rev. B* **87**, 214303 (2013).
 - ²³ G. Fugallo, M. Lazzeri, L. Paulatto, F. Mauri, *Phys. Rev. B* **88**, 045430 (2013).
 - ²⁴ P. Giannozzi et al., *J. Phys.: Condens.Matter*, **21**, 395502 (2009); www.quantum-espresso.org.
 - ²⁵ J. P. Perdew, K. Burke and M. Ernzerhof, *Phys. Rev. Lett.* **77**, 3865 (1996).
 - ²⁶ S. Grimme, *J. Comp. Chem.* **27**, 1787 (2006).
 - ²⁷ R. Shaltaf, X. Gonze, M. Cardona, R. K. Kremer, and G. Siegle, *Phys. Rev. B* **79**, 075204 (2009).
 - ²⁸ H. Monkhorst, and J. D. Pack, *Phys. Rev. B* **13**, 5188 (1976).
 - ²⁹ X. Gonze and J.-P. Vigneron, *Phys. Rev. B* **39**, 13120 (1989).
 - ³⁰ M. Omini and A. Sparavigna, *Il Nuovo Cimento D* **19**, 1537 (1997).
 - ³¹ C. A. Ratsifaritana and P. G. Klemens, *Int. J. Thermophys.* **8**, 737 (1987).
 - ³² D. Campi, D. Donadio, G. C. Sosso, J. Behler, and M. Bernasconi *J. Appl. Phys.* **117**, 015304 (2015).
 - ³³ J. Goldak, C.S. Barrett, D. Innes, and W. Youdelis, *J. Chem. Phys.* **44**, 3323 (1966).
 - ³⁴ T. Chattopadhyay, J. Boucherle, and H. Von Schnering, *J. Phys. C* **20**, 1431 (1987).
 - ³⁵ A. H. Edwards, A. C. Pineda, P. A. Schultz, M. G. Martin, A. P. Thompson, H. P. Hjalmarson, and C. J. Umrigar, *Phys. Rev. B* **73**, 045210 (2006).
 - ³⁶ A. J. Bevolo, H. R. Shanks, and D. E. Eckels, *Phys. Rev. B* **13**, 3523 (1976).
 - ³⁷ L. Paulatto, I. Errea, M. Calandra, and F. Mauri, *Phys. Rev. B* **91**, 054304 (2015).
 - ³⁸ T. L. Anderson, and H. B. Krause, *Acta Crystallogr. B* **30**, 1307 (1974).

- ³⁹ G. C. Sosso, G. Miceli, S. Caravati, J. Behler, and M. Bernasconi, *Phys. Rev. B* **85**, 174103 (2012).
- ⁴⁰ G. C. Sosso, S. Caravati, and M. Bernasconi, *J. Phys. : Condens. Matter* **21**, 095410 (2009).
- ⁴¹ LandoltBörnstein 1983 Antimony telluride (Sb_2Te_3) phonon dispersion, phonon frequencies Numerical Data and Functional Relationships in Science and Technology (New Series, Group III (Condensed Matter), vol 41 (Semiconductors), subvolume C (Non Tetrahedrally Bonded Elements and Binary Compounds I)) ed O Madelung, M Schulz and H Weiss (New York: Springer) doi:10.1007/10681727_1054
- ⁴² G. C. Sosso, S. Caravati, C. Gatti, S. Assoni and M. Bernasconi, *J. Phys. : Condens. Matter* **21**, 245401 (2009).
- ⁴³ A. Zunger, S. H. Wei, L. G. Ferreira, and G. E. Bernard, *Phys. Rev. Lett.* **65**, 353 (1990).
- ⁴⁴ A. D. Becke, *J. Chem. Phys.* **77**, 5648 (1993); J. P. Perdew and W. Wang, *Phys. Rev. B* **45**, 13244 (1992).
- ⁴⁵ D Campi, E Baldi, G Graceffa, G C Sosso, and M. Bernasconi, *J. Phys.; Condens. Matter* **27**, 175009 (2015).
- ⁴⁶ B.-S. Lee, J. R. Abelson, S. G. Bishop, D.-H. Kang, B.-K. Cheong, and K.-B. Kim, *J. Appl. Phys.* **97**, 093509 (2005).
- ⁴⁷ M. Methfessel and A. T. Paxton, *Phys. Rev. B* **40**, 3616 (1989).
- ⁴⁸ D. G. Cahill, S. K. Watson and R. O. Pohl, *Phys. Rev. B* **46**, 802 (1992).
- ⁴⁹ T. Tsafack, E. Piccinini, B.-S. Lee, E. Pop, and M. Rudan, *J. Appl. Phys.* **110**, 063716 (2011).